Journal of Power Sources 196 (2011) 3186–3194

Contents lists available at ScienceDirect

Journal of Power Sources

journal homepage: www.elsevier.com/locate/jpowsour

Computational modeling of a direct propane fuel cell

H. Khakdaman[a,b], Y. Bourgault[c], M. Ternan[a,b,d,*]

[a] Department of Chemical and Biological Engineering, University of Ottawa, 161 Louis-Pasteur, Ottawa, K1N 6N5 Canada
[b] Center for Catalysis Research and Innovation, University of Ottawa, 30 Marie-Curie St., Ottawa, K1N 6N5 Canada
[c] Department of Mathematics and Statistics, University of Ottawa, 585 King Edward Avenue, Ottawa, Ontario, K1N 6N5 Canada
[d] EnPross Incorporated, 147 Banning Road, Ottawa, K2L 1C5 Canada

ARTICLE INFO

Article history:
Received 4 October 2010
Received in revised form
16 November 2010
Accepted 22 November 2010
Available online 26 November 2010

Keywords:
PEM fuel cell
Direct propane fuel cell
Mathematical modeling
Interdigitated flow field

ABSTRACT

The first two dimensional mathematical model of a complete direct propane fuel cell (DPFC) is described. The governing equations were solved using FreeFem software that uses finite element methods. Robin boundary conditions were used to couple the anode, membrane, and cathode sub-domains successfully. The model showed that a polytetrafluoroethylene membrane having its pores filled with zirconium phosphate (ZrP–PTFE), in a DPFC at 150 °C performed much the same as other electrolytes; Nafion, aqueous H_3PO_4, and H_2SO_4 doped polybenzimidazole, when they were used in DPFCs. One advantage of a ZrP–PTFE at 150 °C is that it operates without liquid phase water. As a result corrosion will be much less severe and it may be possible for non-precious metal catalysts to be used. Computational results showed that the thickness of the catalyst layer could be increased sufficiently so that the pressure drop between the reactant and product channels of the interdigitated flow fields is small. By increasing the width of the land and therefore the reactant's contact time with the catalyst it was possible to approach 100% propane conversion. Therefore fuel cell operation with a minimum concentration of propane in the product stream should be possible. Finally computations of the electrical potential in the ZrP phase, the electron flux in the Pt/C phase, and the overpotential in both the anode and cathode catalyst layers showed that serious errors in the model occurred because proton diffusion, caused by the proton concentration gradient, was neglected in the equation for the conservation of protons.

1. Introduction

Several advantages are obtained when hydrocarbons are the fuel used directly at the anode of a fuel cell. The capital cost for processing equipment needed to produce hydrogen or methanol can be eliminated. The infrastructure to deliver hydrocarbons is already in place (natural gas pipelines in urban areas and commercial trucking systems for delivery of LPG and diesel fuel in rural areas). A substantial additional capital cost for delivery systems would be required if hydrogen and/or methanol were to become equally accessible. Furthermore, the conversion energy inefficiencies (e.g. endothermic heat required for steam reforming) are eliminated. Storage of liquid hydrocarbons is also much more energy efficient and convenient than that of hydrogen.

Although hydrocarbons have many advantages they also have one major disadvantage compared to hydrogen or methanol. Hydrocarbon reaction rates (current densities) in fuel cells are more than one order of magnitude slower than those of hydrogen or methanol.

Extensive fuel cell research, using hydrocarbons as the fuel was performed in the 1959–1968 period. That work has been summarized in three reviews, Liebhafsky and Cairns [1], Bockris and Srinivasan [2], and Cairns [3]. Different hydrocarbons such as normal paraffins (methane to n-hexadecane), olefins (ethylene, propylene and 1-butene), gasoline and diesel have been investigated as the fuel cell feed. An overview [1] of work during the 1959–1968 period shows that: (1) normal alkanes have been the most frequently used fuels, (2) most electrolytes were aqueous acids, (3) platinum has been the favourite electrocatalyst, and (4) cell potentials have been low, which is a serious drawback.

Work in our laboratory is directed toward improving the viability of direct hydrocarbon fuel cells by combining several strategies.

The first is the selection of a membrane that is capable of operation at a temperature of at least 150 °C to ensure that no water is present in the liquid phase. The membrane is composed of two components, a porous polytetrafluoroethylene (PTFE) that contains zirconium phosphate (ZrP) in its pores. It was chosen for this research because it has demonstrated reasonable performance when operated at a 120 °C in a hydrogen fuel cell [4]. In the absence of liquid water, corrosion problems are expected to

* Corresponding author at: EnPross Incorporated, Development, 147 Banning Road, Ottawa, K2L 1C5 Canada. Tel.: +1 613 831 8080; fax: +1 613 831 5458.
E-mail address: ternan@sympatico.ca (M. Ternan).

0378-7753/$ – see front matter © 2010 Elsevier B.V. All rights reserved.
doi:10.1016/j.jpowsour.2010.11.115

Nomenclature

A_{Pt}	platinum surface area per catalyst volume ($m^2_{Pt}\,m^{-3}_{catalyst}$)
A_{CAT}	specific surface area of catalyst support (Vulcan carbon) in the anode and cathode ($m^2_{catalyst}\,g^{-1}_{catalyst}$)
c_G	total-concentration of the gas phase ($mol\,m^{-3}$)
$c_{i,ELY}$	concentration of charged-species i in electrolyte ($mol\,m^{-3}$)
D_i	diffusion coefficient of species i ($cm^2\,s^{-1}$)
D_p	effective particle diameter (μm)
F	Faraday's constant, 96485 ($C\,mol^{-1}_{charge}$)
$f_{Pt/CAT}$	fraction of catalyst support surface area covered by platinum ($m^2_{Pt}\,m^{-2}_{catalyst}$)
$\Delta G^{\ddagger}$	activation energy for the exchange current density ($kJ\,mol^{-1}$)
j	volumetric current density; rate of production of proton in electrode ($A\,m^{-3}_{catalyst}$)
$\boldsymbol{j}$	current density, vector quantity ($A\,m^{-2}_{electrode\ face\ area}$)
j_0	exchange current density at operating conditions ($A\,m^{-2}_{Pt}$)
j_{0-ref}	reference exchange current density at the reference conditions ($A\,m^{-2}_{Pt}$)
J	total current density ($mA\,cm^{-2}$)
J_i	diffusion flux of species i ($mol\,m^{-2}\,s^{-1}$)
L_W	land width in the flow field (mm)
MW_i	molecular weight of species i ($g\,mol^{-1}$)
n	normal direction
$\boldsymbol{N}_{i,ELY}$	flux of species i in electrolyte, vector quantity ($mol\,cm^{-2}\,s^{-1}$)
p_i	partial pressure of species i (Pa)
P	total pressure (Pa)
R	universal gas constant ($J\,mol^{-1}\,K^{-1}$)
S_i	consumption rate of the reactant species i ($mol\,m^{-3}\,s^{-1}$)
T	temperature (K)
Th	thickness of catalyst layers and membrane (μm)
t	time (s)
$\boldsymbol{u}$	velocity of gas mixture, vector quantity ($m\,s^{-1}$)
$\boldsymbol{u}_{ELY}$	velocity of electrolyte ($m\,s^{-1}$)
u_i	mobility of species i ($cm^2\,mol\,J^{-1}\,s^{-1}$)
u_n	velocity of gas mixture in normal direction ($m\,s^{-1}$)
x	Cartesian coordinate
y	Cartesian coordinate
y_i	mole fraction of species i in the gas phase
z	moles of electron in anode and cathode reactions ($mol_{electrons}\,mol^{-1}_{propane}$)
z_i	charge number of species i ($mol_{charge}\,mol^{-1}_{species}$)

Greek letters

α_A and α_C	anodic and cathodic charge transfer coefficients
α_1, α_2 and α_3	relaxation parameters in boundary conditions
η	overpotential (V)
ε	volume fraction
ρ	mass density ($kg\,m^{-3}$)
ρ_{CAT}	apparent bulk density of catalyst support ($g_{catalyst}\,m^{-3}_{catalyst}$)
ρ_i	mass density of species i ($kg\,m^{-3}$)
μ_G	dynamic viscosity of gas mixture ($kg\,m^{-1}\,s^{-1}$)
ν_i	stoichiometric coefficient of species i
σ	ionic conductivity ($S\,m^{-1}$)
Φ	electrical potential (V)
Φ_{Pt-EQ}	equilibrium potential of conductor phase (V)
Φ_{ELY-EQ}	equilibrium potential of electrolyte phase (V)
$\Delta\Phi_{CELL}$	cell potential difference (V)
$\sum(v_i)$	sum of the atomic volumes for each of the i species ($m^3\,kg\,atom^{-1}$)

Subscripts and superscripts

A	anode
av	phase-averaged quantity
C	cathode
C_3	propane
C_3Ox	propane oxidation reaction on Pt catalyst
CO_2	carbon dioxide
ELY	electrolyte phase in the anode or cathode catalyst layers
EQ	equilibrium state
G	gas mixture
H_2O	water
i	species in gas phase; propane, water, CO_2 and O_2
ML	membrane layer
n	normal direction
O_2	oxygen
O_2Rd	oxygen reduction reaction on platinum catalyst
Pt	platinum catalyst
ref	reference conditions

decrease dramatically and it may be possible to replace precious metal catalysts with less expensive ones. The model described here uses Pt/C catalysts for both anode and cathode because reaction rate data were available in the literature. If the ZrP–PTFE membrane investigated here is shown to be suitable, then a future search for non-precious metal catalysts maybe appropriate.

The use of interdigitated flow fields has at least two desirable features [5,6]. First, the partial pressure of the reactants all along the feedstock channels can be maintained constant at their values in the feedstock. In the more common serpentine flow-fields, reactants are diluted by the products that enter the same channel. Therefore, the partial pressures of the reactants decrease as reaction proceeds and more products are produced. Second, the width of the catalyst layer can be increased thereby increasing the reactor length and the residence time in contact with the catalyst. In principle, the conversion could approach 100%, thereby minimizing the concentration of unreacted hydrocarbons in the product stream.

This work describes the first two-dimensional model of a complete direct propane fuel cell (DPFC). Both anode and catalyst layers contain two solid phases, a Pt/C phase that conducts electrons and a ZrP phase that conducts protons. The ZrP–PTFE membrane conducts protons through the ZrP that fills the pores. There are no other components in the membrane layer. The following reactions proceed in a DPFC assuming complete propane conversion. The electrical potential values shown are the standard reversible electrochemical potentials at 25 °C:

$$\text{Anode reaction}: C_3H_8 + 6H_2O = 3CO_2 + 20H^+ + 20e^- \quad \phi_{AN} = 0.136\,V$$

$$\text{Cathode reaction}: 5O_2 + 20H^+ + 20e^- = 10H_2O \quad \phi_{CA} = 1.229\,V$$

$$\text{Overall reaction}: C_3H_8 + 5O_2 = 3CO_2 + 4H_2O \quad \Delta\phi_{CELL} = 1.093\,V$$

The generation of electrical energy in rural areas is our target application for DPFCs. The cost of delivering electrical energy to rural areas is substantially greater than to urban areas, because longer transmission lines are required to serve a comparatively

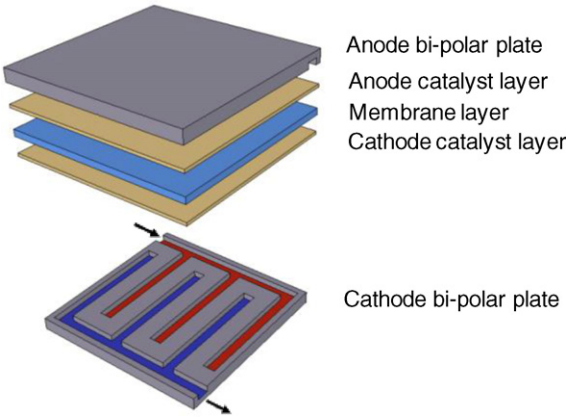

Fig. 1. A direct propane fuel cell with interdigitated flow field.

small number of customers. Therefore more costly fuel cells can be justified for rural areas than for urban areas. In addition, the infrastructure to deliver liquefied petroleum gas (LPG) or propane to rural areas already exists, because LPG is one of the fuels used for heating in rural areas.

2. Model development

A schematic of a typical DPFC has been illustrated in Fig. 1. The cell is composed of two bi-polar plates, two catalyst layers and a membrane layer. The cathode bi-polar plate in Fig. 1 shows two sets of channels, one for reactants and one for products that are connected to each other through the catalyst layer. In addition the catalyst layers can be thicker when using interdigitated flow fields than when using serpentine flow fields. Thicker catalyst layers make it possible to have a better dispersion of catalyst (more reaction sites).

A cross sectional view of the cell is shown in Fig. 2. Because of the symmetry of the interdigitated flow field, the modeling domain is defined to be from the middle of a feed channel to the middle of its adjacent product channel. It contains the membrane electrode assembly (MEA) including both the anode and cathode catalyst layers and the membrane layer.

2.1. Governing equations

Anode and cathode catalyst layers are composed of three phases: reactants and products in the gas phase, solid ZrP electrolyte, and solid catalyst (Pt/C). The membrane layer also contains solid ZrP as well as PTFE. Because different variables in different phases are of interest, a multi-fluid volume averaging method has been used [8]. In this method, spatial averaging is performed for each single phase within a multiphase control volume. Also, the extensive phase-averaged quantities are related to the intensive phase-averaged amounts and phase fractions. For example, the phase-averaged density for the gas phase in a control volume can be calculated by multiplying the gas phase density by its volume fraction in the control volume, as written in Eq. (1):

$$\rho_{G,av} = \varepsilon_G \times \rho_G \tag{1}$$

Therefore, phase-averaged quantities were used in the governing equations for the solid and gas phases. Conservation of mass, momentum, and species for the gas phases in the anode and cathode are shown in Tables 1 and 2, respectively. These tables also include equations for the conservation of protons in the ZrP solid phase in each of the layers. The conservation of protons is the only equation that has to be solved for the membrane layer. Because of the relatively large electron conductivity of the Pt/C solid catalyst (the electron conducting phase), conservation of electrons in the Pt/C phase was not considered. Instead it is assumed that the electrical potential in the Pt/C phase was constant.

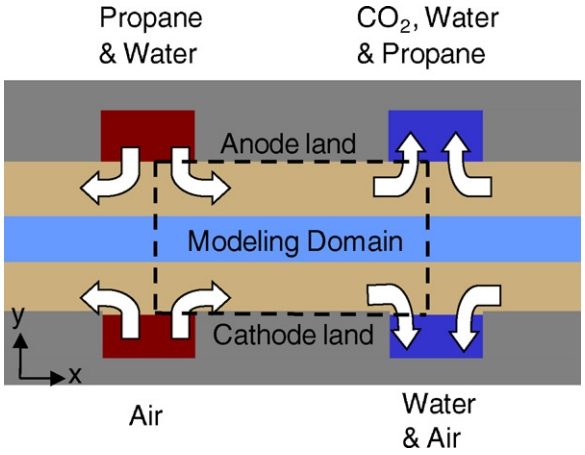

Fig. 2. Modeling domain containing anode and cathode catalyst layers and electrolyte layer.

Table 1
List of equations for the anode.

Equations	Eq. no.
Conservation of mass: $\frac{\partial(\varepsilon_G\rho_G)}{\partial t} = -\nabla\cdot(\varepsilon_G\rho_G\boldsymbol{u}) - \frac{MW_{C_3}j_A}{zF} - \frac{6MW_{H_2O}j_A}{zF} + \frac{3MW_{CO_2}j_A}{zF}$	(2)
Conservation of momentum: $-\nabla P = 150\left[\frac{\mu_G(1-\varepsilon_G)^2}{D_p^2\varepsilon_G^3}\right]\boldsymbol{u}$	(3)
Conservation of non-charged species: Gas phase: $\frac{\partial(\varepsilon_G c_G y_{C_3})}{\partial t} = -\nabla\cdot(\varepsilon_G c_G \boldsymbol{u} y_{C_3}) + \nabla\cdot(J_{C_3}) - \frac{j_A}{zF}$	(4)
$\frac{\partial(\varepsilon_G c_G y_{H_2O})}{\partial t} = -\nabla\cdot(\varepsilon_G c_G \boldsymbol{u} y_{H_2O}) + \nabla\cdot(J_{H_2O}) - \frac{6j_A}{zF}$	(5)
Conservation of charge: For ionic current: $\nabla\cdot(\varepsilon_{ELY}\sigma_{ELY}\nabla\Phi_{ELY,A}) = -j_A$	(6)
Butler–Volmer equation: $j_A = j_{0,A}A_{Pt}\left[\exp\left(\frac{\alpha_A F\eta_A}{RT}\right) - \exp\left(\frac{-\alpha_C F\eta_A}{RT}\right)\right]$	(7)
where, $j_{0,A} = j_{0-ref,}^{C_3Ox}\left(\frac{p_{C3}}{p_{C3,ref}}\right)\exp\left[\left(\frac{\Delta G_{C_3Ox}^{\ddagger}}{R}\right)\left(\frac{1}{T_{ref}} - \frac{1}{T}\right)\right]$	(8)
$\eta_A = \Delta\Phi_A - \Delta\Phi_{EQ,A} = (\Phi_{Pt,A} - \Phi_{ELY,A}) - (\Phi_{Pt-EQ,A} - \Phi_{ELY-EQ})$	(9)

Table 2
List of equations for the cathode.

Equations	Eq. no.
Conservation of mass: $\frac{\partial(\varepsilon_G\rho_G)}{\partial t} = -\nabla\cdot(\varepsilon_G\rho_G\boldsymbol{u}) - \frac{5MW_{O_2}j_C}{zF} + \frac{10MW_{H_2O}j_C}{zF}$	(10)
Conservation of momentum: $-\nabla P = 150\left[\frac{\mu_G(1-\varepsilon_G)^2}{D_p^2\varepsilon_G^3}\right]\boldsymbol{u}$	(11)
Conservation of species: Gas phase: $\frac{\partial(\varepsilon_G c_G y_{O_2})}{\partial t} = -\nabla\cdot(\varepsilon_G c_G \boldsymbol{u} y_{O_2}) + \nabla\cdot(J_{O_2}) - \frac{5j_C}{zF}$	(12)
$\frac{\partial(\varepsilon_G c_G y_{N_2})}{\partial t} = -\nabla\cdot(\varepsilon_G c_G \boldsymbol{u} y_{N_2}) + \nabla\cdot(J_{N_2})$	(13)
Conservation of charge: For ionic current: $\nabla\cdot(\varepsilon_{ELY}\sigma_{ELY}\nabla\Phi_{ELY,C}) = -j_C$	(14)
Butler–Volmer equation: $j_C = j_{0,C}A_{Pt}\left[\exp\left(\frac{\alpha_A F\eta_C}{RT}\right) - \exp\left(\frac{-\alpha_C F\eta_C}{RT}\right)\right]$	(15)
where, $j_{0,C} = j_{0-ref,}^{O_2Rd}\left(\frac{p_{O_2}}{p_{O_2,ref}}\right)\exp\left[\left(\frac{\Delta G_{O_2Rd}^{\ddagger}}{R}\right)\left(\frac{1}{T_{ref}} - \frac{1}{T}\right)\right]$	(16)
$\eta_C = \Delta\Phi_C - \Delta\Phi_{EQ,C} = (\Phi_{Pt,C} - \Phi_{ELY,C}) - (\Phi_{Pt-EQ,C} - \Phi_{ELY-EQ})$	(17)

Table 3
Parameters for Eqs. (8) and (16) [10].

Parameter	Anode	Cathode
T_{ref} (K)	423	298
P_{ref} (kPa)	101.3	101.3
j_{0-ref} (A cm^{-2} Pt)	1.0×10^{-8}	3.8×10^{-13}
$\Delta G^{\ddagger}$ (kJ mol^{-1})	90	92

The first term of the Ergun equation has been used to describe momentum conservation because the catalyst layers are essentially packed beds. Conservation of non-charged species in the gas phase accounts for diffusion, convection and reaction phenomena. The consumption rate of the reactant species, S_i, is related to the volumetric current density, j, through Faraday's law:

$$S_i = \frac{-\nu_i j}{zF} \tag{18}$$

with j given by the Butler–Volmer equation:

$$j = j_0 A_{Pt} \left[\exp\left(\frac{\alpha_A F\eta}{RT}\right) - \exp\left(\frac{\alpha_C F\eta}{RT}\right) \right] \tag{19}$$

where j_0, the exchange current density, is a function of the reference exchange current density, j_{0-ref}, and operating temperature and pressure. The reference exchange current density for propane oxidation on platinum has been reported in the literature [9]. In order to calculate the exchange current density at different temperatures the Arrhenius-type expression suggested by Psofogiannakis et al. [10] was used:

$$j_0 = j_{0-ref} \exp\left[\left(\frac{\Delta G^{\ddagger}}{R}\right) \left(\frac{1}{T_{ref}} - \frac{1}{T}\right) \right] \tag{20}$$

The parameters required to calculate j_0 for propane oxidation at the anode and oxygen reduction at the cathode are reported in Table 3. The final expressions for the exchange current densities at the anode and cathode are shown in Eqs. (8) and (16).

Three mechanisms, diffusion, migration, and convection, are involved in the transport of protons through the electrolyte phase as shown by Nernst–Planck equation [11]:

$$\boldsymbol{N}_{i,ELY} = -z_i u_i F c_{i,ELY} \nabla \Phi_{ELY} - D_i \nabla c_{i,ELY} + c_{i,ELY} \boldsymbol{u}_{ELY} \tag{21}$$

The first term in Eq. (21) describes the migration of protons for which the driving force is the electrical potential gradient. The second term describes the diffusive flux of protons for which the driving force is the concentration gradient (related to the chemical potential gradient). The final term describes the convective flux of protons that is caused by the bulk motion of the solvent. For the stationary membrane of the present system, $\boldsymbol{u}_{ELY} = 0$. Some of the more rigorous models have included both migration and diffusion terms [12–14]. However, the majority of PEM fuel cell models neglect the concentration gradient and therefore the diffusion term [15–17]. In other words the majority of PEM fuel cell models combine migration and diffusion into a single term for which the driving force is the electrical potential gradient. This work also ignored the concentration gradient and described proton flux as a single term for which the electrical potential gradient was the driving force. That choice had some undesirable consequences that will be discussed in a subsequent section of this communication.

Movement of charged species in the ZrP electrolyte phase produces current that can be quantified by Eq. (22) [18]:

$$\boldsymbol{j} = F \Sigma_i z_i \boldsymbol{N}_{i,ELY} \tag{22}$$

Substitution of Eq. (21) in Eq. (22) for a stationary membrane in the absence of a concentration gradient results in:

$$\boldsymbol{j} = -\sigma_{ELY} \nabla \Phi_{ELY} \tag{23}$$

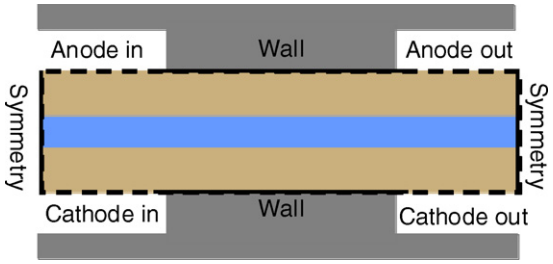

Fig. 3. Boundaries in the modeling domain.

where

$$\sigma_{ELY} = F^2 \sum z_i^2 u_i c_{i,ELY} \tag{24}$$

is the conductivity of the ZrP electrolyte.

Electro-neutrality of the entire domain can be expressed by Eq. (25):

$$\sum \nabla \cdot \boldsymbol{j}_i = 0 \tag{25}$$

As the charged species are electrons and protons, Eq. (25) at any location in the domain can be written as:

$$-\nabla \cdot \boldsymbol{j}_{H+} = \nabla \cdot \boldsymbol{j}_{e-} = j \tag{26}$$

where j is rate of reaction (volumetric current density) given by the Butler–Volmer equation. Therefore, an equation for the conservation of protons in the absence of electrochemical reactions, which is the situation in the membrane layer, can be written as:

$$\nabla \cdot (\sigma_{ELY} \nabla \Phi_{ELY,ML}) = 0 \tag{27}$$

The combination of Eqs. (23) and (26) is shown for the anode as Eq. (6) and for the cathode as Eq. (14).

2.2. Boundary conditions

Fig. 3 shows the four types of boundary conditions that were used to model the domain; inlets, outlets, walls of the lands, and symmetry boundaries. Table 4 shows the values for the boundary conditions. The Ergun equation was solved using the boundary condition values in Table 4 for the velocities at the inlets (calculated from inlet flow rates) and the atmospheric pressure boundary condition at the outlets. At the interface between the catalyst layers and lands (referred to as the wall), the flux of gaseous species is zero. That is also true for the proton flux because protons are not transferred from the catalyst layers to the lands. Instead a potential difference is set between lands for electrons. The zero flux condition has been applied at the symmetry boundaries, assuming the fuel cell repeats by reflection through these boundaries at the left and right of the computational domain. This reflection is a natural assumption for interdigitated channels.

The feed composition is known at the inlet of the catalyst layers. It is assumed that no change in the composition of gaseous species will occur after the gas mixture leaves the catalyst bed. Therefore, the gradient of the composition is zero in the direction normal to the catalyst surface at the outlet boundaries. Also, the electrical current is zero in the normal direction of the inlet and outlet boundaries, both for protons and electrons.

2.3. Model input parameters

The parameters used for the simulations are shown in Table 5. To calculate platinum surface area per catalyst volume, A_{Pt}, that is used in the Butler–Volmer equation it is assumed that a fraction,

Table 4
List of boundary conditions for the modeling domain.

Anode inlet:			
$u_y = 0.001–0.005\ m\ s^{-1}$		$\frac{\partial \Phi_{ELY}}{\partial y} = 0$	
$y_{C3} = 0.10$		$y_{H_2O} = 0.90$	
Anode outlet:			
$P = 101.3$ kPa	$\frac{\partial \Phi_{ELY}}{\partial y} = 0$	$\frac{\partial y_{C_3}}{\partial y} = 0$	$\frac{\partial y_{H_2O}}{\partial y} = 0$
Cathode inlet:			
$u_y = 0.001–0.005\ m\ s^{-1}$		$\frac{\partial \Phi_{ELY}}{\partial y} = 0$	
$y_{O_2} = 1.00$		$y_{H_2O} = 0.00$	
Cathode outlet:			
$P = 101.3$ kPa	$\frac{\partial \Phi_{ELY}}{\partial y} = 0$	$\frac{\partial y_{O_2}}{\partial y} = 0$	
Anode/land interface (wall):			
$u_y = 0$	$\frac{\partial \Phi_{ELY}}{\partial y} = 0$	$\frac{\partial y_i}{\partial y} = 0$	$\Phi_{Pt} = 0.15–0.50$ V
Cathode/land interface (wall):			
$u_y = 0$	$\frac{\partial \Phi_{ELY}}{\partial y} = 0$	$\frac{\partial y_i}{\partial y} = 0$	$\Phi_{Pt} = 0.9–1.2$ V
Zero flux boundaries:			
$u_x = 0$	$\frac{\partial \Phi_{ELY}}{\partial x} = 0$		$\frac{\partial y_i}{\partial x} = 0$
Anode/membrane interface:			
$\varepsilon_{ELY,A}\sigma_{ELY,A}\left(\frac{\partial \Phi_{ELY,A}}{\partial y}\right) = \sigma_{ML}\left(\frac{\partial \Phi_{ML}}{\partial y}\right)$			$\Phi_{ELY,A} = \Phi_{ML}$
$u_n = 0$	$\frac{\partial y_i}{\partial n} = 0$		
Cathode/membrane interface:			
$\sigma_{ML}\left(\frac{\partial \Phi_{ML}}{\partial y}\right) = \varepsilon_{ELY,C}\sigma_{ELY,C}\left(\frac{\partial \Phi_{ELY,C}}{\partial y}\right)$			$\Phi_{ELY,C} = \Phi_{ML}$
$u_n = 0$	$\frac{\partial y_i}{\partial n} = 0$		

$f_{Pt/CAT}$, of catalyst support surface area, A_{CAT}, is covered by platinum. Therefore A_{Pt} can be calculated using Eq. (28):

$$A_{Pt} = f_{Pt/CAT} \times A_{CAT} \times \rho_{CAT} \tag{28}$$

2.4. Numerical procedure

The software used to solve the two-dimensional partial differential equations is FreeFEM++, which was developed by Hecht et al. [19]. It is a open-source software based on the Finite Element Method which is capable of handling multi-variables, multi-equations, two and three-dimensional systems and steady state or time dependent problems. In addition, the results calculated using FreeFEM++, can be easily exported to ParaView software [20] for post-processing. ParaView is open-source software used for visualization that is quite powerful.

Table 5
Operational, electrochemical and design parameters for simulations.

Property	Value
Temperature, T	423 K
Pressure, P	101.3 kPa
Charge transfer coefficients, α_A and α_C	1.0 [10]
Electrolyte ionic conductivity for ZrP–PTFE, σ_{ELY}	$5.0\ S\ m^{-1}$
Equilibrium potential of conductor phase at the anode, $\Phi_{Pt-EQ,A}$	0.136 V [1]
Equilibrium potential of conductor phase at the cathode, $\Phi_{Pt-EQ,C}$	1.229 V
Equilibrium potential of electrolyte phase, Φ_{ELY-EQ}	0.136 V
Apparent bulk density of catalyst support, ρ_{CAT}	$0.259\ g_{catalyst}\ mL^{-1}_{catalyst}$
Specific surface area of catalyst support in the anode and cathode, A_{CAT}	$255\ m^2_{catalyst}\ g^{-1}_{catalyst}$
Gas phase volume fraction in anode and cathode, ε_G	0.5
Electrolyte phase volume fraction in anode and cathode, ε_{ELY}	0.4
Effective particle diameter in anode and cathode, D_p	5 μm
Land width, L_W	1–6 mm
Anode and cathode thickness, Th_A, Th_C	200–400 μm
Membrane thickness, Th_M	100 μm
Fluid channels width in bi-polar plates	0.4 mm

The partial differential equations and the required boundary conditions discussed in Sections 2.1 and 2.2, respectively, are rewritten into variational form, and discretized by the Finite Element Method in space. The Euler time stepping method is used to discretize the equations in time with all nonlinear reaction terms taken explicitly and linearized differential terms taken implicitly to increase stability. The partial differential equations are solved one after another in a decoupled fashion. Time steps are performed until a steady-state solution of the fully coupled system of nonlinear equations is reached, usually of the order of a few hundred time-steps. Grid independence of the solution was achieved by computing solutions on sufficiently refined meshes.

A special method was required to couple the solutions on all the layers. One of the main difficulties is the solution of the potential equations for protons over the three layers while matching potentials and fluxes of protons at the membrane–catalyst layer interfaces. Moreover, proton fluxes are zero on the exterior boundary of the whole computational domain suggesting that the rate of proton production in the anode is equal to the rate of proton consumption in the cathode. In an attempt to couple the anode with the membrane, and the membrane with the cathode, the anode and the cathode are coupled together as well. A domain decomposition method with Robin boundary conditions on the potential has been employed successfully to solve the potential equations in the anode, membrane and cathode. In the Robin method, linear combinations of the unknown potentials and their fluxes are used as boundary conditions. For example, Eqs. (29) and (30) are used as boundary conditions at the anode/membrane interface to solve potential equations in the anode and membrane domains:

$$\varepsilon_{ELY,A}\sigma_{ELY,A}\left(\frac{\partial \Phi_{ELY,A}}{\partial y}\right) + \alpha_1 \Phi_{ELY,A} = \sigma_{ML}\left(\frac{\partial \Phi_{ML}}{\partial y}\right) + \alpha_1 \Phi_{ML} \tag{29}$$

$$-\sigma_{ML}\left(\frac{\partial \Phi_{ML}}{\partial y}\right) + \alpha_2 \Phi_{ML} = -\varepsilon_{ELY,A}\sigma_{ELY,A}\left(\frac{\partial \Phi_{ELY,A}}{\partial y}\right) + \alpha_2 \Phi_{ELY,A} \tag{30}$$

where α_1 and α_2 are relaxation parameters related to the anode and membrane volume, respectively.

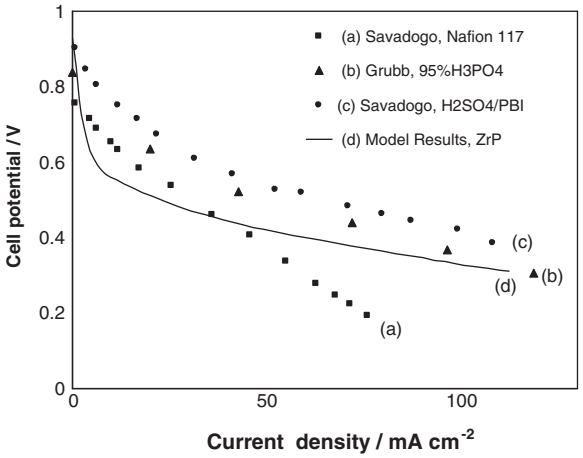

Fig. 4. Polarization curves of direct propane/oxygen fuel cell using Pt anode and cathode: (a) experimental results [21] using Nafion 117 at 95 °C, (b) experimental results [9] using 95% H_3PO_4 at 200 °C, (c) experimental results [21] using H_2SO_4 doped PBI at 95 °C, and (d) the present model results for a solid ZrP–PTFE electrolyte at 150 °C; the base case-study.

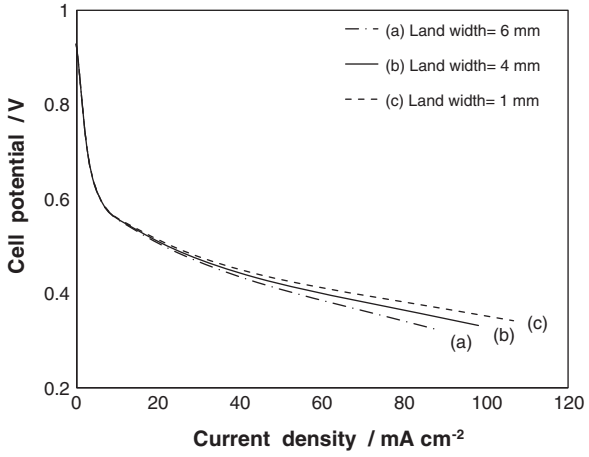

Fig. 5. Polarization curves of direct propane/oxygen fuel cell showing model results for catalyst thickness of 300 μm at different land widths.

The layers were solved sequentially, with a single iteration of the coupling method at each time step. A Newton method was used to force equal proton production/consumption rates at the anode and cathode.

2.5. Model validation

The model predicts the performance of a DPFC having interdigitated flow fields and a solid ZrP–PTFE electrolyte operating at temperatures of at least 150 °C. In order to validate the model, two sets of published experimental data have been chosen for comparison purposes. Savadogo and Rodriguez Varela [21] reported polarization curves for DPFCs with several modified solid electrolytes operating at low temperatures. Grubb and Michalske [9] presented polarization curve data for DPFCs using phosphoric acid as the electrolyte operating at temperatures as high as 200 °C.

Fig. 4 compares the modeling results with the experimental data. Graph (a) in Fig. 4 shows the performance of a DPFC with a non-modified Nafion 117 solid electrolyte. Although Nafion has a proton conductivity approaching 10 S m^{-1} [25], it has to be used at temperatures of 80 °C or less. At elevated temperatures both the liquid phase water content of Nafion membranes and their performance decline substantially. Graph (b) in Fig. 4 shows Grubb's best results obtained using a DPFC having a liquid phosphoric acid electrolyte. Because there are no experimental data for direct propane fuel cells having zirconium phosphate electrolytes, a comparison was made between results from our model having a zirconium phosphate electrolyte and experimental data obtained with other electrolytes. The comparison in Fig. 4 indicates that the zirconium phosphate electrolyte would have results that are somewhat comparable to the other electrolytes. Although the variation in results among the electrolytes shown in Fig. 4 for direct propane fuel cells are significant, they are minor when they are compared to results from a hydrogen fuel cell.

The different results obtained with the different electrolytes may be related to the various electrolyte conductivities. The proton conductivity of phosphoric acid electrolyte depends on its concentration and on the operating temperature. Dobos has reported the proton conductivity of phosphoric acid at 298 K and its temperature variations [22]. Proton conductivity of a 95% H_3PO_4 at 200 °C is equal to 35 S m^{-1}. The best experimental conductivity achieved for ZrP in our laboratory was approximately 5 S m^{-1}. The greater proton conductivity values for Nafion 117 and 95% H_3PO_4 result in higher cell potentials at low current densities compared to the ZrP–PTFE electrolyte modeled in this study. However, as current densities increases, the experimental cell potential results decrease more rapidly for Nafion 117 and 95% H_3PO_4 compared to the ZrP–PTFE model results. One explanation is that both Nafion and 95% H_3PO_4 have at least a partial liquid film around the Pt/C catalyst sites. This leads to larger Ohmic losses compared to a DPFC with solid ZrP–PTFE electrolyte at 150 °C where there is no liquid phase water and no liquid film is present to create a diffusion resistance.

The model prediction in Fig. 4 indicates that a ZrP–PTFE membrane will give a polarization curve that is generally similar to those obtained with H_3PO_4, Nafion, and H_2SO_4 doped polybenzimidazole (PBI). The difference is that ZrP–PTFE does not need liquid phase water, whereas the others do. Acceptable operation in the absence of liquid water suggests that the highly corrosive environment can be avoided and that a search for a non-precious metal catalyst to replace Pt/C may be warranted.

3. Results and discussion

The model was employed for two purposes. The effects of some of the physical characteristics of the flowfields (land width) and the MEA (catalyst layer thickness) were examined. It was also used in an attempt to understand proton transport in the ZrP electrolyte phase and electron transport in the Pt/C phase. In addition, the variation of some of the gas phase variables was investigated. These studies are described in this section.

Fig. 5 shows the effect of land width, i.e. the distance between inlet and outlet channels, on the cell performance. It is apparent that increasing the land width has a small negative effect on the polarization curve. As the reactants flow from an inlet channel towards its adjacent outlet channel within the catalyst layer, the partial pressure of the reactants decreases and that leads to a lower reaction rate and a smaller current production. This can be explained by the dependence of exchange current density on the partial pressure of the reactants in the Butler–Volmer equation.

A major concern about the interdigitated flow fields is their higher pressure-drop compared to the conventional serpentine flow fields. However, it has been shown that with interdigitated flow fields, thicker catalyst layers have smaller pressure drops [7]. Large pressure drops are a serious drawback for interdigitated flow fields. This perception is correct for serpentine flow fields using conventional anode catalyst layers of 40 μm. However, by increasing the thickness of the anode catalyst layer to 400 μm, the pressure drop along the land width will decrease. Moreover, an increase in the catalyst thickness results in an improvement in the polariza-

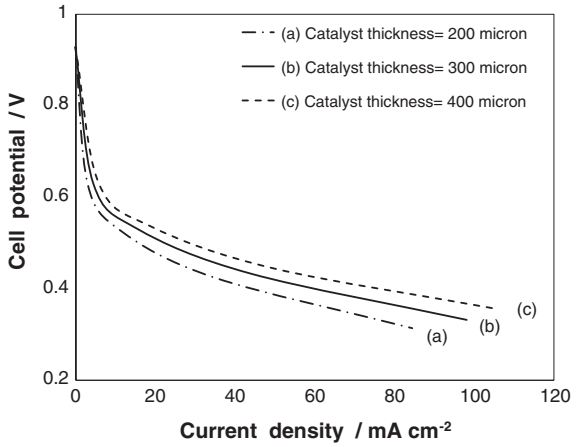

Fig. 6. Polarization curves of direct propane/oxygen fuel cell showing model results for the land width of 4 mm at different catalyst thicknesses.

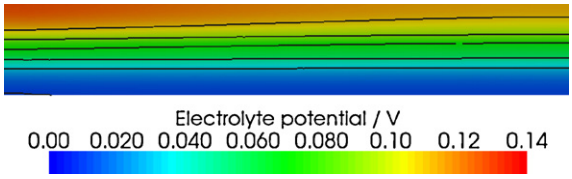

Fig. 7. Potential profile for the ZrP phase within the cathode catalyst layer, the anode catalyst layer, and the membrane layer.

tion curve as can be seen in Fig. 6. Improved dispersion of the metal catalyst should be obtained using a thicker catalyst layer without changing the total amount of catalyst used. An increased dispersion would correspond to a larger number of reaction sites.

Fig. 7 shows the two-dimensional variation of the electrical potential in the ZrP phase of the entire domain, that is the anode catalyst layer, the membrane layer, and the cathode catalyst layer. A cross-section of Fig. 7 is shown in Fig. 8, where the electrical potential in the ZrP phase is compared with that in the Pt/C phase.

Fig. 8 shows the following MEA profiles in the *y*-direction (as defined in Fig. 2): (a) a comparison of the electrical potential in the Pt/C solid phase with that in the ZrP phase for the anode catalyst layer, (b) the same comparison as in (a) but for the cathode catalyst layer, and (c) the electrical potential profile of the ZrP phase in the membrane layer. As the electrical conductivity in the Pt/C phases is very high, the electrical potential in both of the Pt/C phases in

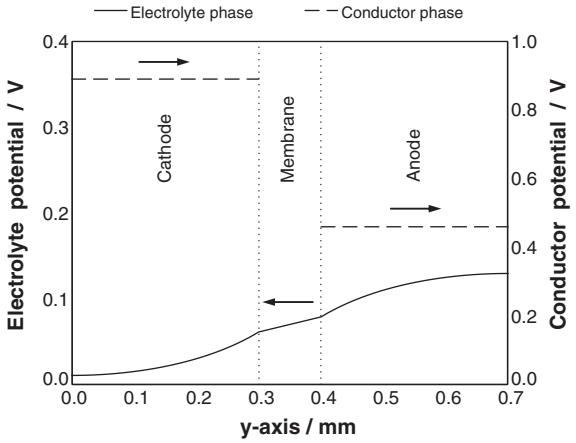

Fig. 8. Potential profiles in the *y*-direction for the ZrP and Pt/C phases located at the middle of the domain *x*-direction for the cathode and anode catalyst layers and membrane layer. The arrows point in the direction of the ordinate scale that applies to each of the three curves.

their respective anode and cathode layers are almost constant, as shown by the horizontal dashed lines in Fig. 8. However, the electrical potential in the ZrP phase varies according to Eqs. (6) and (14), as shown by the solid line in Fig. 8.

The model uses this electrical potential gradient to account for proton migration from the ZrP phase in the anode catalyst layer, through the ZrP phase in the membrane layer, and into the ZrP phase in the cathode catalyst layer. As mentioned previously neglecting the diffusion term in Eqs. (6) and (14) is a common assumption used in most PEM fuel cell models. Reasonable predictions of the fuel cell polarization curve were obtained using this assumption, as shown in Figs. 4–6. However, one of the undesirable consequences of this assumption is that the slope of electrical potential in the ZrP phases in the three layers is positive. It should be negative. The correct sign of the slope can be understood from the following reasoning: the potential gradient between anode and cathode drives electrons from the Pt/C phase of the anode to the Pt/C phase of the cathode via the external circuit. If the fuel cell had an aqueous electrolyte, the electrical double layer would have described the difference in electrical potential between the catalyst layers and the electrolyte. Since ZrP has semi-conducting properties [23], the difference in electrical potential between Pt/C and ZrP will be described by a space charge region [24]. As a result the electrical potential in the ZrP phases will be directly related to the electrical potentials in the Pt/C phases that are shown as the dashed lines in Fig. 8. Therefore the electrical potential in the ZrP phase of the anode catalyst layer must be less than that in the ZrP phase of the cathode catalyst layer. Therefore opposite trend, shown in Fig. 8, cannot be correct. Since negatively charged electrons are driven from the anode to the cathode by the electrical potential gradient (in the Pt/C phases), the corresponding gradient (in the ZrP phases), when correctly calculated, must provide a driving force for positively charged protons from the cathode to the anode. As the electrochemical reaction proceeds protons will accumulate (in the ZrP phase) at the anode until the proton concentration gradient from the anode to the cathode is sufficient to overcome the electrical potential gradient (in the ZrP phases). When that condition is attained, electrons will flow through the ZrP phases from the anode to the cathode. The conclusion is that Fig. 8 has an incorrect sign for the slope of the electrical potential gradient (in the ZrP phase). If the model had included the diffusion term with its concentration gradient in Eq. (21) then the sign of the slope in Fig. 8 would have been correct.

It is worth mentioning that the solid line in Fig. 8 for the electrolyte phase potential shows that the condition of zero proton flux at the lands has been satisfied, and coupling at the membrane/catalyst layers interfaces has been done perfectly.

Fig. 9 shows that the overpotential predicted by the model at both the membrane/catalyst interfaces is greater than that at their corresponding lands. This prediction by the model is incorrect, as can be seen from the following reasoning at the anode: the overpotential at the anode is given by Eq. (9), $\eta_A = (\Phi_{Pt,A} - \Phi_{ELY,A}) - (\Phi_{Pt-EQ,A} - \Phi_{ELY-EQ}) = (\Phi_{Pt,A} - \Phi_{ELY,A})$ when the equilibrium potential of the ZrP electrolyte, Φ_{ELY-EQ} is been defined to be equal to the equilibrium potential in the Pt/C catalyst $\Phi_{Pt-EQ,A}$. According to Fig. 8, the potential difference $\Phi_{Pt,A} - \Phi_{ELY,A}$ is greater at the anode catalyst–membrane interface than at the anode catalyst–land interface. That is consistent with the overpotential in Fig. 9. However, if proton diffusion driven by the proton concentration gradient had been included in the model, then the electrical potential gradient in the ZrP phases in Fig. 8 would have been reversed. That would also reverse the slope of the overpotential gradients in Fig. 9.

Fig. 10a and b shows the magnitude and direction of proton and electron fluxes, respectively. Protons and electrons are produced in the anode and consumed in the cathode. Protons travel through the ZrP–PTFE electrolyte phase from anode to cathode, as shown in

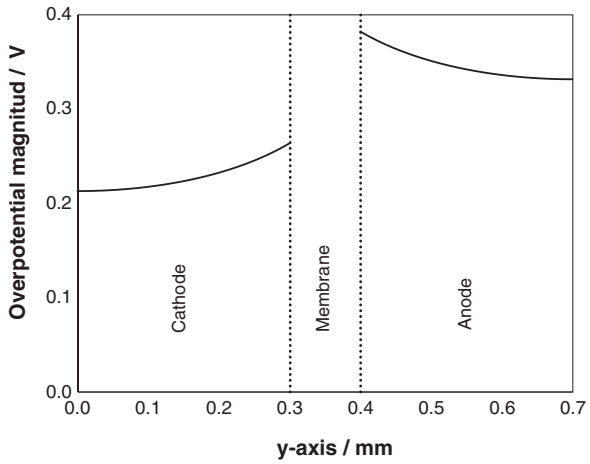

Fig. 9. Overpotential profile at the anode and cathode.

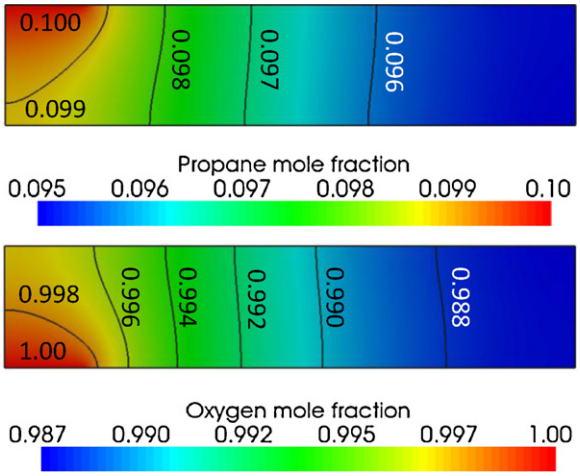

Fig. 11. Propane and oxygen mole fraction at the anode and cathode, respectively.

Fig. 10a. Protons are produced throughout the anode catalyst layer. The arrow's length in Fig. 10a correctly indicates that the proton flux increases as the position in the anode's *y*-direction changes from the anode catalyst–land interface to the membrane–anode catalyst interface.

Electrons travel from anode to cathode via the external circuit although there is a very small amount of electronic current through the membrane layer. Electron transport also occurs in the ZrP phase of the catalyst layers. It is the electron transport in the ZrP phase that is shown in Fig. 10b. Neglecting the diffusion term in the proton conservation equation caused the direction of the electron flux, in Fig. 10b, to be incorrect, as was described previously.

Fig. 11 shows the variation in the propane and oxygen mole fractions at the anode and cathode, respectively. The concentrations of the reactants decrease along the land as the reactants flow from the inlet to the outlet. Therefore, changing the land's width can control the conversion of the reactants. This is an important benefit of interdigitated flow fields for DPFCs. Even if the feed channels

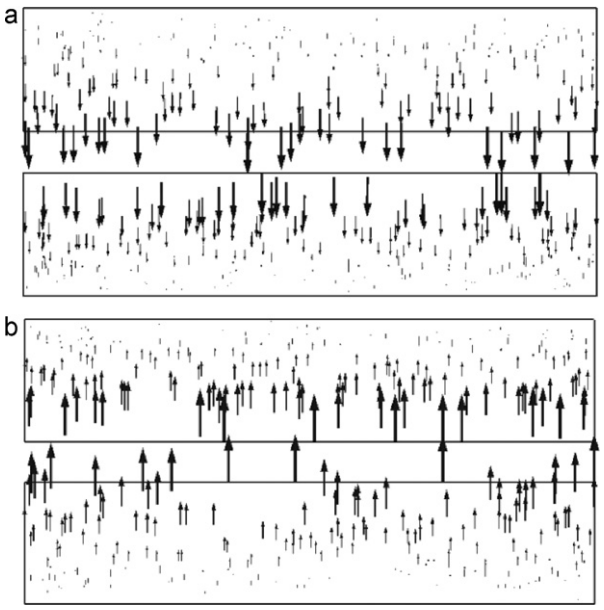

Fig. 10. (a) Protonic current from anode to cathode in electrolyte phase. The vectors length indicates the current magnitude which varies from 0 to 120 mA cm^{-2} in this case and (b) electronic current from cathode to anode in electrolyte phase. The vectors length indicates the current magnitude which varies from 0 to 2*e* − 14 mA cm^{-2} in the same case as Fig. 10a.

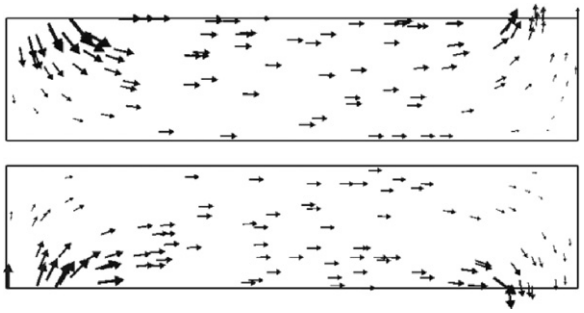

Fig. 12. Velocity vectors showing movement of fluid in the anode and cathode catalyst layers.

are dead-ended so that all of the reactants must flow through the catalyst layer, as shown in Fig. 1, it would be undesirable for unreacted propane to contaminate the product gas stream that ideally should consist only of carbon dioxide and water vapour. The water concentration at the anode entrance was specified to exceed the stoichiometric ratio because it is needed for both reaction and to assist proton transport (osmotic drag).

Fig. 12 shows the velocity vectors in the gas phase of the anode and cathode catalyst layers. Arrows in *x*-direction on the land represent a slip flow regime in the catalyst layer. This suggests that the Ergun equation describes momentum conservation appropriately, since the catalyst layers have been modeled as packed beds

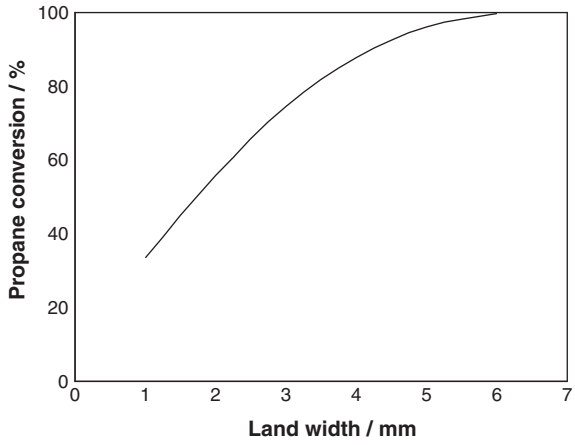

Fig. 13. Propane conversion at different anode and cathode land widths.

and flow though a packed bed is possible even at the wall of a land. Finally, the small velocity vectors indicate poor catalyst turnover frequency.

Fig. 13 shows that the propane conversion increases as the land width increases. The fact that 100% propane conversion can be approached with interdigitated flow fields is important. As explained previously unreacted propane in the product stream would be undesirable. A 100% conversion result is unlikely with a serpentine flow field. In a serpentine flow field the carbon dioxide products would mix with the hydrocarbon feedstock. The smaller propane concentration in the channels of serpentine flow fields would decrease the driving force that pushes the hydrocarbons into the catalyst layer.

4. Conclusion

The performance predicted for a DPFC at 150 °C using a polytetrafluoroethylene membrane with its pores filled with zirconium phosphate (ZrP–PTFE) was similar to experimental results obtained with Nafion, aqueous H_3PO_4, and H_2SO_4 doped polybenzimidazole electrolytes, when they were used in DPFCs. Because a ZrP–PTFE membrane operating at 150 °C does not require water in the liquid phase, corrosion will be much less severe, and the use of non-precious metal catalysts may be possible. It was found that the thickness of the catalyst layer could be increased sufficiently so that the pressure drop between the reactant and product channels of interdigitated flow fields was small. By increasing the width of the lands and therefore the reactant's contact time with the catalyst it was possible to approach 100% propane conversion, thereby ensuring that there will be a minimum concentration of propane in the product stream from the fuel cell. Finally neglecting the diffusion term in the equation for the conservation of protons causes serious errors in computations of the electrical potential in the ZrP phase, the electron flux in the Pt/C phase, and the overpotential in both the anode and cathode catalyst layers.

Acknowledgements

Financial assistance is gratefully acknowledged. A Discovery Grant was awarded from the Canadian federal government's Natural Sciences and Engineering Research Council. A project within the Ontario Fuel Cell Research and Innovation Network (OFCRIN) was funded both by the Ontario provincial government's Ontario Research Fund and by the Network's industrial sponsors. One of us (H.K.) is grateful to the Ontario government for the award of an Ontario Graduate Scholarship.

References

[1] H.A. Liebhafsky, E.J. Cairns, Fuel Cells and Fuel Batteries, Wiley, New York, 1968, pp. 458–523.
[2] J.O. Bockris, S. Srinivasan, Electrochemical Combustion of Organic Substances, McGraw-Hill, New York, 1969, pp. 357–411.
[3] E.J. Cairns, Adv. Electrochem. Electrochem. Eng. 8 (1971) 337–391.
[4] Y. Si, R. Jiang, J.C. Lin, H.R. Kunz, J.M. Fenton, J. Electrochem. Soc. 151 (2004) A1820–A1824.
[5] W. Yan, S. Mei, C. Soong, Z. Liu, D. Song, J. Power Sources 160 (2006) 116–122.
[6] W. Yan, C. Yang, C. Soong, F. Chen, S. Mei, J. Power Sources 160 (2006) 284–292.
[7] H. Khakdaman, Y. Bourgault, M. Ternan, Ind. Eng. Chem. Res. 49 (2010) 1079–1085.
[8] A. Faghri, Y. Zhang, Transport Phenomena in Multiphase Systems, Elsevier/Academic Press, Boston, 2006, p. 244.
[9] W.T. Grubb, C.J. Michalske, J. Electrochem. Soc. 111 (1964) 1015–1019.
[10] G. Psofogiannakis, Y. Bourgault, B.E. Conway, M. Ternan, J. Appl. Electrochem. 36 (2006) 115–130.
[11] A.Z. Weber, J. Newman, Chem. Rev. 104 (2004) 4679–4726.
[12] A.Z. Weber, J. Newman, J. Electrochem. Soc. 151 (2004) A311–A325.
[13] J.J. Baschuk, X. Li, Appl. Energy 86 (2009) 181–193.
[14] J.J. Baschuk, X. Li, Int. J. Hydrogen Energy 35 (2010) 5095–5103.
[15] P.C. Sui, S. Kumar, N. Djilali, J. Power Sources 180 (2008) 410–422.
[16] T. Berning, D.M. Lu, N. Djilali, J. Power Sources 106 (2002) 284–294.
[17] Z.H. Wang, C.Y. Wang, K.S. Chen, J. Power Sources 94 (2001) 40–50.
[18] J. Newman, K.E. Thomas-Alyea, Electrochemical Systems, third ed., Wiley-Interscience, New Jersey, U.S.A., 2004, p. 275.
[19] Hecht F, Pironneau O, LeHyaric A, Ohtsuka K. FreeFEM++ Version 3.9. Available at: http://www.freefem.org/ff++/, 2010.
[20] ParaView 3.8-Open Source Scientific Visualization. Available at: http://www.paraview.org/, 2010.
[21] O. Savadogo, F.J. Rodriguez Varela, J. New Mater. Electrochem. Syst. 4 (2001) 93–97.
[22] D. Dobos, Electrochemical Data: A Handbook for Electrochemists in Industry and Universities, Elsevier, New York, 1975, p. 339.
[23] O.P. Panwar, A. Kumar, R. Amet, S.C. Amet, Macedonian J. Chem. Chem. Eng. 27 (2008) 133–139.
[24] A. Many, Y. Goldstein, N.B. Grover, Semiconductor Surfaces, North-Holland, Amsterdam, 1971, p. 128.
[25] M. Doyle, G. Rajendran, in: W. Vielstich, A. Lamm, H.A. Gasteiger (Eds.), Handbook of Fuel Cells, vol. 3, Wiley, England, 2003, p. 373.